

# Dynamic Optical Localization of a Mobile Robot Using Kalman Filtering-Based Position Prediction

Jason N. Greenberg , *Student Member, IEEE*, and Xiaobo Tan , *Fellow, IEEE*

**Abstract**—Autonomous mobile robots operating in areas with poor GPS and wireless coverage (e.g., underwater) must rely on alternative localization and communication approaches. In this article, we present an light-emitting diode (LED) based system that achieves simultaneous localization and communication (SLAC), where the line-of-sight (LOS) requirement for communication is exploited to extract the relative bearing of the communicating parties for localization. By using Kalman filtering to obtain the mobile robot's predicted position, the system is able to reduce the overhead of establishing the LOS and, therefore, significantly improve on the quality of the localization. The proposed design of the optical localization system is presented and its effectiveness is demonstrated with extensive simulation and experimentation in a two-dimensional setting, consisting of a mobile robot and two stationary base nodes.

**Index Terms**—Bearing-based localization, dynamic localization, Kalman filtering, light-emitting diode (LED) based communication.

## I. INTRODUCTION

LOCALIZATION is an essential requirement for the operation of mobile systems (such as robots and vehicles) and sensor networks. GPS is arguably the most common tool for acquiring location. However, in many applications (such as underwater exploration [1] and indoor navigation), GPS signals are not available. A number of alternative localization approaches have been developed for mobile robots operating in areas with poor GPS service, such as computer vision-based simultaneous localization and mapping (SLAM) [2]–[5] and inertial measurement-based dead reckoning [6]–[8]. SLAM typically requires significant and expensive computing resources for processing the visual or Lidar images [9], while dead reckoning suffers from sensor drift issues [5], [10], [11].

Manuscript received January 26, 2020; accepted March 5, 2020. Date of publication March 13, 2020; date of current version October 14, 2020. Recommended by Technical Editor Z. Liu. This work was supported by the National Science Foundation under Grants ECCS 1446793 and IIS 1734272. (Corresponding author: Jason Neil Greenberg.)

The authors are with the Smart Microsystems Laboratory, Department of Electrical and Computer Engineering, Michigan State University, East Lansing, MI 48824 USA (e-mail: green108@egr.msu.edu; xbtan@egr.msu.edu).

Color versions of one or more of the figures in this article are available online at <http://ieeexplore.ieee.org>.

Digital Object Identifier 10.1109/TMECH.2020.2980434

Although there are other localization methods that can work without GPS signals, their use underwater tends to be achieved through acoustic signals. While acoustic techniques are currently predominant in underwater localization and communication, they present a number of challenges because of limited bandwidth, long propagation delays, and multipath effect, which result in low data rates and low signal reception reliability [12], [13]. Moreover, devices that implement acoustic-based methods tend to be bulky and power-hungry, making them unsuitable for small underwater robots with limited resources [1].

Optical communication systems based on light-emitting diodes (LEDs) are an up-and-coming alternative to acoustic-based methods. In recent years, LED systems have shown promise in high-rate, low-power underwater communication over short-to-medium distances [14], [15]. For example, the system developed by Brundage [16], which used a Titan blue lighting LED, achieved communication rates of roughly 1 Mb/s at a distance of 13 m, while Doniec [17] demonstrated data rates of 4 Mb/s at a distance of 50 m with their communication system, AquaOptical II, that used an array of 18 Luxeon Rebel LEDs for the transmitter. However, a downside of LED-based communication is the requirement of near line of sight (LOS) between the transmitter and the receiver. The latter challenge has been addressed in several ways, including the use of redundant transmitters/receivers [18]–[21] and active alignment [15], [22], [23].

Indoor LED-based localization and communication systems have been developed by using visible light communication (VLC) systems, in which the overhead lights used to illuminate the room can also be used as the transmission medium for both data and localization purposes [24]. Nguyen *et al.* [25] developed a VLC localization approach that integrates the angle of arrival and received signal strength of the light to compute the location, getting a minimum simulated error of 10 cm. Qiu *et al.* [24] achieved a localization accuracy of 0.56 m using a fingerprint matching approach, where fingerprints are a mapping of position and the light intensities of each light in the environment, and each light transmits a unique beacon pattern allowing the localizing robot to associate a light intensity with a particular overhead fixture. While VLC-based localization and visible light positioning approaches are an alternative to radio-frequency methods indoors and can work underwater in theory, they are not practical for a typical aquatic environment due to the difficulty in illuminating the significantly larger and more complex environment.

An underwater LED-based localization and communication system was presented by Rust and Asada in [20]. This approach relies on a nonlinear light intensity model to calculate the distance between the transmitting LED and the receiving photodiode. However, such an approach is prone to error since light intensity depends on both distance and receiver–transmitter alignment. The method in [20] also uses a photodiode array to determine the angle of the light source, which increases the size and complexity of the system.

### A. Main Contribution

In this article, we present an alternative concept of LED-based simultaneous localization and communication (SLAC), where the LOS requirement in LED-based communication is exploited to extract the relative bearing of the two communicating parties. Such bearing information for a mobile robot, with respect to multiple nodes with known locations (called base nodes or beacons), can then be used to infer the location of the robot via triangulation. In particular, we consider the single-transmitter–single-receiver setup with active alignment for the LED communication system [21], [22] due to its advantages in small footprint and low power, compared with systems with multiple transmitters and/or multiple receivers. However, the very directional nature of such a setup, along with the mobile nature of the target (robot), presents a significant challenge in establishing the LOS for bearing measurement and communication.

A key contribution of this article is the proposal of Kalman filter-based position prediction for the mobile robot, to facilitate the establishment and maintenance of the LOS between the base nodes and the robot. Extensive simulation and experiments have been conducted to evaluate the proposed approach, with a comparison to an alternative approach not using Kalman filtering-based location prediction. In particular, the robustness of the proposed approach with respect to the LOS angle measurement error and the uncertainty in the robot’s initial position is assessed in simulation. The simulated results show that the system can localize effectively when the angle measurements have an error with a standard deviation of  $3.0^\circ$  or less. Experimental results show that the system is able to consistently localize the mobile node and maintain tracking of the robot indefinitely. In contrast, a version of the approach that does not use the Kalman filtering-based position prediction is only able to localize the mobile node for a relatively small number of steps of the trajectory before losing track of its position.

Some preliminary results of the proposed approach were reported at the 2016 and 2017 ASME Dynamic Systems and Control Conferences [26], [27]. In [26], the LED-based SLAC concept with simulation and rudimentary experimentation was first introduced; in [27], a more systematic procedure of executing the experiments was introduced to obtain and maintain the LOS. This article represents a significant extension and improvement over [26] and [27]; in particular, the enhancements have included improved hardware for the control and tracking of the mobile robot, revised algorithms involving additional linear filters for extracting the LOS angle with higher accuracy, new simulation results evaluating the robustness of the proposed approach with

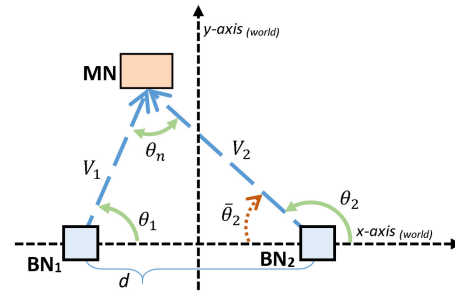


Fig. 1. Illustration of the problem setup.

respect to measurement noise and initial estimate uncertainty, and new experimental results including the comparison with an alternative approach.

The rest of this article is organized as follows. In Section II, the proposed scheme, including the basic problem setup and the Kalman filtering-based prediction algorithm, is presented. In Section III, the operational protocol for the system is described in detail. Simulation results are provided in Section IV, followed by experimental evaluation results in Section V. Finally, Section VI concludes this article.

## II. OVERVIEW OF THE APPROACH

In this section, we outline the major elements of this article. Section II-A provides a more detailed description of the problem setup, and Section II-B describes how the Kalman filter is used for coordinating the LOS angle prediction and scanning.

### A. Problem Setup

To simplify the discussion, in this article, the localization approach is considered in the two-dimensional space. It is assumed that each node is equipped with an optical transceiver comprised of an LED transmitter and a photodiode receiver, and that the transceiver is able to rotate a full  $360^\circ$ . Furthermore, the node is able to identify at any particular moment the angle at which its transceiver is facing with respect to a reference direction such as the east axis identified by a magnetic compass. Consider a three-node network composed of a pair of base nodes (with known locations) and a mobile node to be localized, as illustrated in Fig. 1. Through the LOS measurement, the base nodes, denoted as  $BN_1$  and  $BN_2$ , respectively, determine the bearing angles of the mobile node (MN) with respect to a common  $x$ -axis, denoted as  $\theta_1$  and  $\theta_2$ .

The location of the MN can then be found using the locations of  $BN_1$  and  $BN_2$  and the bearing angles  $\theta_1$  and  $\theta_2$  as

$$\begin{bmatrix} n_x \\ n_y \end{bmatrix} = \begin{bmatrix} B_{1x} + |V_1| \cos \theta_1 \\ B_{1y} + |V_1| \sin \theta_1 \end{bmatrix} \quad (1)$$

where  $[n_x, n_y]^T$  is the position vector of the mobile node MN,  $B_{1x}$  and  $B_{1y}$  are the respective  $x$  and  $y$  coordinates for  $BN_1$ , and  $|V_1|$  is the magnitude of vector  $V_1$ , as shown in Fig. 1, and

is obtained using the Laws of Sines as

$$|V_1| = \frac{d \sin(\bar{\theta}_2)}{\sin(\theta_n)}. \quad (2)$$

Here  $d$  is the distance between  $\text{BN}_1$  and  $\text{BN}_2$ ,  $\bar{\theta}_2$  is the complement of  $\theta_2$ ,  $\bar{\theta}_2 = 180^\circ - \theta_2$ , and  $\theta_n$  is the angle corresponding to the side  $\text{BN}_1\text{--BN}_2$  within the  $\text{MN--BN}_1\text{--BN}_2$  triangle,  $\theta_n = \theta_2 - \theta_1$ .

Although this localization process seems simple, the task is involved, especially when the target is mobile. The challenge comes from the need to have sufficient synchronization and coordination among all three nodes to produce proper LOS measurements. Otherwise the mobile node could be “spotted” (via LOS) too infrequently, not at all, or not nearly simultaneously by both base nodes. Another challenge results from the error in the measured  $\theta_1$  and  $\theta_2$ —purely relying on the algebraic calculation (1) will lead to highly variable (instead of smooth) estimated trajectories for the mobile node MN. To help address both challenges, Kalman filtering is proposed for predicting and estimating the location of the MN, based on the measured location computed via (1). In particular, the prediction of the MN location is exploited to significantly reduce the effort searching for LOS and, thus, enable efficient and accurate localization. The Kalman filtering algorithm is presented next.

### B. Kalman Filtering Algorithm

Kalman filtering is a powerful and computationally efficient technique for estimating the state of linear systems with Gaussian noises [28]–[31], and it has been widely adopted for estimation and control in various applications including robotics. The main focus of this article is the maintenance of the LOS between the base nodes and the mobile node. This is achieved using a Kalman filter to predict the future location of the robot in order to generate anticipated angles for transceiver orientation. The mobile node’s dynamics are assumed to be sufficiently described by a constant velocity model corrupted with Gaussian noise, since it is not practical for the base nodes to have precise prior knowledge of the mobile node’s movement. While other filtering schemes can be potentially used, our assumption enables the use of computationally efficient Kalman filtering for predicting the mobile node’s position. As demonstrated later in this article, these predictions are crucial for efficient establishment of LOS measurement and, thus, the success of the localization scheme. The dynamics for the mobile node can be represented as

$$\mathbf{n}_{k+1} = \mathbf{n}_k + \mathbf{v}_k \Delta_k + w_{1,k} \quad (3)$$

$$\mathbf{v}_{k+1} = \mathbf{v}_k + w_{2,k} \quad (4)$$

where  $\mathbf{n}_k = [n_{x,k}, n_{y,k}]^T$  and  $\mathbf{v}_k = [v_{x,k}, v_{y,k}]^T$  are the position and velocity vectors of the mobile node at the  $k$ th time instance,  $w_{1,k}$  and  $w_{2,k}$  are independent, zero-mean, white Gaussian noises, and  $\Delta_k$  is the  $k$ th sampling interval. The observation  $\mathbf{z}_k$  is the noise-corrupted location measurement, computed based on (1) and (2), calculated as

$$\mathbf{z}_k = \mathbf{n}_k + w_{3,k} \quad (5)$$

where  $w_{3,k}$  is assumed to be white, zero-mean Gaussian, and independent of the process noises  $w_{1,k}$  and  $w_{2,k}$ .

The state vector  $\hat{\mathbf{x}}_k$  of the Kalman filter is defined as

$$\hat{\mathbf{x}}_k = [\hat{n}_x, \hat{n}_y, \hat{v}_x, \hat{v}_y]^T \quad (6)$$

where  $[\hat{n}_x, \hat{n}_y]^T$  and  $[\hat{v}_x, \hat{v}_y]$  are the estimated position and velocity, respectively, of the mobile node. The equations for the implementation of the Kalman filter, which are standard [28], are omitted here for brevity.

At time  $k$ , the base nodes perform an angular search process to ultimately generate the observation  $\mathbf{z}_k$  to be used in the state estimate update. The angular search process for each base node is centered about the anticipated values of  $\theta_1$  and  $\theta_2$  (recall Fig. 1) computed from the position component of the predicted state estimate.

In particular, these anticipated angles  $\hat{\theta}_{1,k}$ ,  $\hat{\theta}_{2,k}$  are computed by using

$$\hat{\theta}_{i,k} = \cos^{-1} \left( \frac{V_{b_i} \cdot V_{m_i}}{|V_{b_i}| |V_{m_i}|} \right), \quad \text{for } i = 1, 2 \quad (7)$$

where

$$V_{b_1} = \begin{bmatrix} 0 \\ 0 \end{bmatrix} - \begin{bmatrix} B_{1x} \\ B_{1y} \end{bmatrix} \quad (8)$$

$$V_{b_2} = \begin{bmatrix} B_{2x} \\ B_{2y} \end{bmatrix} \quad (9)$$

$$V_{m_i} = \begin{bmatrix} \hat{n}_x^- \\ \hat{n}_y^- \end{bmatrix} - \begin{bmatrix} B_{ix} \\ B_{iy} \end{bmatrix}, \quad \text{for } i = 1, 2. \quad (10)$$

Here,  $[B_{1x}, B_{1y}]^T$  and  $[B_{2x}, B_{2y}]^T$  are the locations of the base nodes  $\text{BN}_1$  and  $\text{BN}_2$ , respectively, and  $V_{b_i} \cdot V_{m_i}$  is the dot product between vectors  $V_{m_i}$  and  $V_{b_i}$ . The mobile node, in the meantime, will use its predicted position to calculate the angular locations of the base nodes relative to itself, and focus its light along these angles during the angular search.

### III. SYSTEM IMPLEMENTATION

The proposed localization method uses the following five-step procedure.

- 1) *Synchronization*: The mobile node waits until it receives an optical message from one of the base node. The transmitted message contains the latest state estimate from the Kalman filter, i.e., both the position and velocity of the mobile node.
- 2) *Movement*: Upon receiving the message, the mobile node moves along its predetermined trajectory for a fixed amount of time and stops.
- 3) *Measurement*: The mobile node uses its recently received state estimate and orientation data to approximate its current position and the angular locations of the base nodes. It will then use this information to shine its LED light at the base nodes. On the other hand, the base nodes use the state estimate to predict the mobile node’s next position and the corresponding angles  $\hat{\theta}_{1,k+1}$  and  $\hat{\theta}_{2,k+1}$

from (7) to (10) so each base node can scan the light coming from the mobile node.

- 4) *Update*: After scanning, the collected angles  $\theta_1$  and  $\theta_2$  are used to generate the observed position  $\mathbf{z}_k$  through (1) and (2), which is then used to update the state vector.

- 5) *Repeat*: Repeat Steps 1–4.

At the start of the program, before the first synchronization sequence, it is assumed that all of the nodes have knowledge of the initial position and velocity of the mobile node, but such knowledge could have error. This article will study the impact of the initial estimate error on the system performance. The mobile node's stop-and-go movement ensures that its position is the same for each of the base node's scans. This is crucial to the localization accuracy since the measurement equations in (1) and (2) assume that the observed angles correspond to the mobile node at a single location. Overall, it is important to point out that, because of the synchronization process, this approach is able to keep a relatively constant sampling time between the measurements despite the stop-and-go movement from the mobile node. In particular, the Kalman filter is able to capture reasonably well the average velocity of the robot.

Finally, we elaborate on the LOS measurement step. The base node scanning procedure is the light searching process executed individually on each base node to obtain the angle of the mobile node relative to that base node. For each base node, the process involves four consecutive sweeps, composed of two pairs of clockwise then counterclockwise sweeps, about the anticipated angle of the mobile node. During regular increments of each of the sweeps, which have a range of  $60^\circ$ , the base node reads and then records the light intensity, associating it with the corresponding orientation of the transceiver at that particular instant. After each sweep, the intensities are processed through a linear filter to smooth out any irregularities in the intensities such as spikes or dips. The angle associated with the median of the group of highest intensities is used as the measured angle of that sweep. This last process helps to mitigate problems associated with moderate light saturation, where a significant span of angles have the same or very similar intensity levels, which obscures the correct angle associated with the direction of the mobile node.

#### IV. SIMULATION RESULTS

Prior to testing the approach experimentally, simulation was conducted to examine the performance of the scheme, especially its robustness against measurement errors and uncertainty in the initial state estimate.

##### A. Simulation Setup

The simulated environment had an area defined as  $x \in [-6, 6]$ ,  $y \in [-11, 1]$  in grid units to mimic the physical space of the experiment, where a grid unit is equivalent to approximately 23 cm. The base nodes  $BN_1$  and  $BN_2$  were positioned at  $[-3, 0]^T$  and  $[3, 0]^T$ , respectively. Two different trajectories for the robot were used. The first was a simple closed loop as shown in Fig. 2, and the second was a figure-8-shaped loop as shown in Fig. 3. Each trajectory was composed of a number

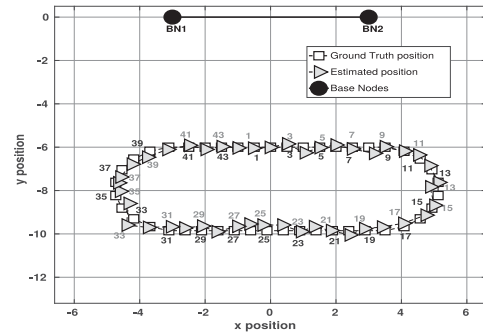


Fig. 2. Comparison of the ground truth and estimated positions for one of the simulated trials using the simple loop trajectory, for the case when the measurement angles of the base nodes are subjected to Gaussian noises with a standard deviation of  $0.5^\circ$ .

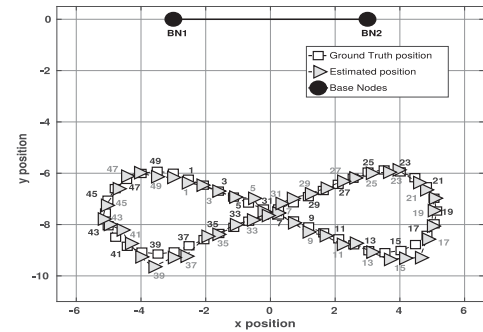


Fig. 3. Comparison of the ground truth and estimated positions for one of the simulated trials using the figure-8-shaped trajectory, for the case when the measurement angles of the base nodes are subjected to Gaussian noises with a standard deviation of  $0.5^\circ$ .

position points, which were used as the ground truth positions in the simulation.

For the simulated measurement step, the orientation value supplied to the mobile node for adjusting its simulated transceiver's direction was obtained by finding the angle between the  $0^\circ$  orientation vector and the vector that points from the previous to the current ground truth position with an added zero-mean Gaussian noise, with a standard deviation of  $0.5^\circ$ , to simulate the imperfection of a physical orientation sensor. The "measured" position in simulation is obtained by triangulation using the simulated measured bearing angles, and the latter are obtained by corrupting the ground-truth bearing angles with independent, zero-mean, white Gaussian noise. The amount of error introduced to these angle measurements was controlled by changing the standard deviation of the Gaussian noise.

##### B. Simulation Results

1) *Impact of Angle Measurement Error*: First the system was analyzed under different levels of angle measurement error. This was achieved by ranging the standard deviation of Gaussian noise introduced to the angle measurements from  $0.5^\circ$  to  $5.0^\circ$  in increments of  $0.5^\circ$ . For each level of standard deviation, 100 trials were conducted. To control the randomness so it would be repeatable, a vector of 100 random seeds was chosen and used for the corresponding trial number for each of the different levels

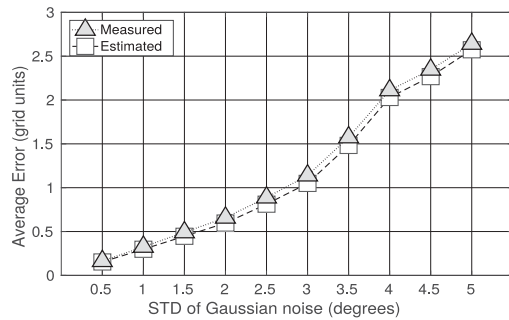


Fig. 4. Average error computed among all of the simulated trials for the simple loop trajectory for varying amounts of standard deviation in the Gaussian noise added to the angular measurements of the base nodes.

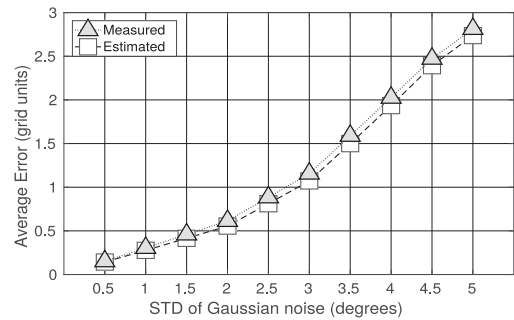


Fig. 6. Average error computed among all of the simulated trials for the figure-8-shaped trajectory for varying amounts of standard deviation in the Gaussian noise added to the angular measurements of the base nodes.

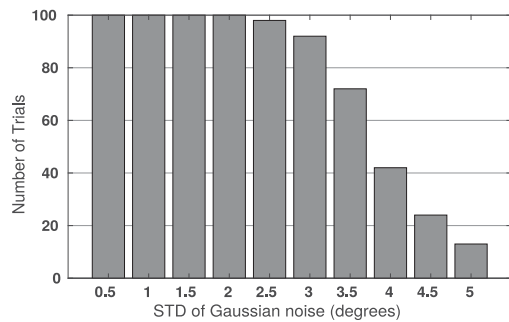


Fig. 5. Bar graph showing how many of the 100 simulated trials for the simple loop trajectory were able to track the complete trajectory for each level of standard deviation of the Gaussian noise added to the angular measurements of the base nodes.

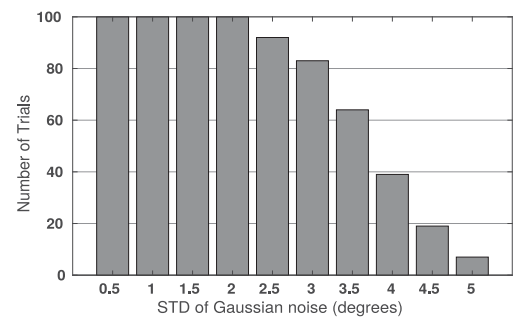


Fig. 7. Bar graph showing how many of the 100 simulated trials for the figure-8-shaped trajectory were able to track the complete trajectory for each level of standard deviation of the Gaussian noise added to the angular measurements of the base nodes.

of standard deviation. Figs. 2 and 3 show the comparison between the ground truth positions and the corresponding Kalman filtering-based estimated positions of the robot in a sample run for the simple loop trajectory and the figure-8-shaped trajectory, respectively, where the angle measurement error has a standard deviation of  $0.5^\circ$ . Fig. 4 shows the average estimated position error and the measured position error among all of the trials for the simple loop trajectory, under each level of standard deviation for the angle measurement error. The estimated (resp., measured) error is the magnitude of the error obtained by comparing the estimated (resp., measured) positions with the corresponding ground truth position. The estimated positions are the output positions from the Kalman filter, whereas the measured positions  $\mathbf{z}_k$  are computed directly from the observed bearing angles. The average errors shown in Fig. 4 were computed using the mean errors from each trial, which were obtained in each trial by averaging the estimated and measured errors from all of the steps of the trajectory the system had reached during that trial. As the standard deviation of the Gaussian noise gets larger, fewer number of trials were able to reach all of the steps of the trajectory. This is reflected in Fig. 5, which shows for each standard deviation how many of the 100 trials were able to reach all the steps. Similarly Fig. 6 shows the average measured and estimated errors from the 100 runs for the figure-8-shaped trajectory, and Fig. 7 shows the number of trials that were fully completed for the figure-8-shaped trajectory.

Collectively the graphs show that the system functions well when the angular measurement error has a standard deviation of  $2.0^\circ$  or less, as it allows the system to track the mobile robot for the entire trajectory with a 100% success rate. The system performance is still largely satisfactory when the standard deviation is about  $3.0^\circ$ . As the standard deviation of the angle measurement error increases, both the measured and estimated position errors increase, as expected, and the number of trials that fail to track the full trajectory rises. We also note that the estimated position is always slightly more accurate than the measured position computed directly from the bearing angles. Finally, the localization performance for the simple loop case is largely comparable to that for the figure-8-shaped case, with slight performance degradation for the latter, suggesting that the proposed scheme is robust to different trajectories for the mobile robot.

2) *Impact of the Error in Initial MN Position Estimation:* The simulation next examined the case where the position of the mobile node initialized into the state vector had varying amount of error from the ground truth. Similar to the angle measurement error case, independent, zero-mean, white Gaussian noises were added to the  $x$  and  $y$  coordinates of the mobile node's initial ground truth position, to obtain the initial estimate of the position. As was done in the previous case, the amount of error introduced to this initial position estimate was controlled by

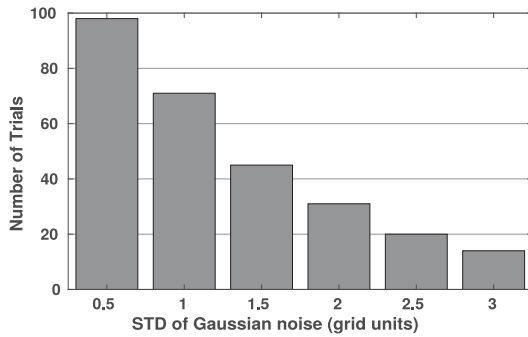


Fig. 8. Bar graph showing how many of the 100 simulated trials for the simple loop trajectory were able to track the complete trajectory for each level of standard deviation of the Gaussian noise added to the initial position of the mobile node.

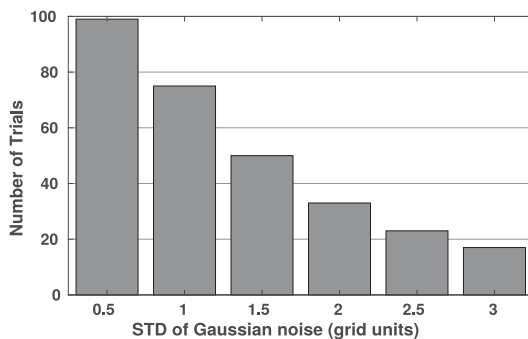


Fig. 9. Bar graph showing how many of the 100 simulated trials for the figure-8-shaped trajectory were able to track the complete trajectory for each level of standard deviation of the Gaussian noise added to the initial position of the mobile node.

changing the standard deviation of the injected noise from 0.5 grid units to 3.0 grid units in increments of 0.5 grid units.

Figs. 8 and 9 show, for each level of the standard deviation, the corresponding numbers of trials completing all steps of the trajectory for the simple loop and figure-8-shaped trajectories, respectively. The trend from these figures indicates that, with an increased error in the initial position estimate, the number of runs completing the full trajectory drops. We note that the system does not have a 100% success rate completing the full trajectories even when the standard deviation is as low as 0.5 grid units. Analysis of simulation data indicates that the latter was caused by the relatively big (larger than 1) realizations of the random variable for those runs.

**3) Justification of Gaussian Noise in Position Measurement Error:** The measurement model (5) assumes a Gaussian noise in the measurement of robot location. This assumption, along with the assumptions made on the process noise, facilitated the use of the Kalman filter for position prediction and estimation. The physical implementation of the position measurement, of course, is through triangulation using the measured bearing angles. Next, we justify the assumption in (5) by evaluating via simulation the measured position error distribution, based on the statistics of error in the bearing angle measurement. In particular, the simulation examined the error distribution in the

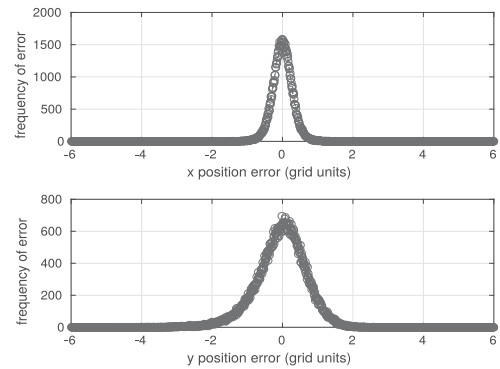


Fig. 10. Error distribution of the mobile node's position in terms of  $x$  and  $y$  when the angular measurements are corrupted with Gaussian noise of zero-mean and a standard deviation of  $1.96^\circ$ .

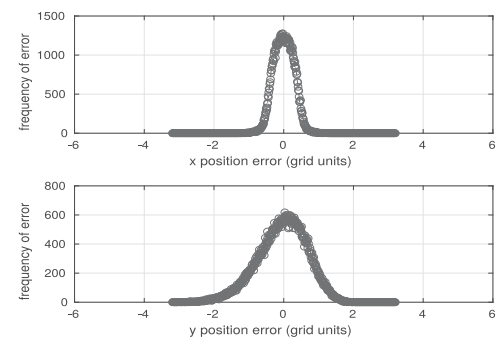


Fig. 11. Error distribution of the mobile node's position in terms of  $x$  and  $y$  when the angular measurements are corrupted with noise that is uniformly distributed between  $[-3.43^\circ, 3.43^\circ]$ .

computed position of the mobile node when the ground truth angular measurements were corrupted with Gaussian noise and uniformly distributed noise. In simulation the same set of 1000 random location points, uniformly distributed throughout the simulation area, were used. For each of these location points, 100 samples of the position error were computed based on the error in bearing angle measurements. Fig. 10 shows the resulting position error distribution when the bearing angle measurement was corrupted with a Gaussian noise with a standard deviation of  $1.96^\circ$ , while Fig. 11 shows the resulting position measurement distribution when the angle measurement was corrupted with a uniform noise randomly distributed between  $[-3.43^\circ, 3.43^\circ]$ . It can be seen that these distributions resemble well the Gaussian distributions. In addition, treating the position measurement error as Gaussian is also supported by the effectiveness of the proposed localization scheme in both simulation results in this section and experimental results in the following section.

## V. EXPERIMENTAL RESULTS

### A. Setup

The transceiver for each node consisted of a single CREE XRE 1 Watt Blue LED (transmitter) and a Blue Enhanced photodiode (receiver) mounted on a circular PCB board that housed the transceiver circuitry developed by Al-Rubaia in [22]. For the

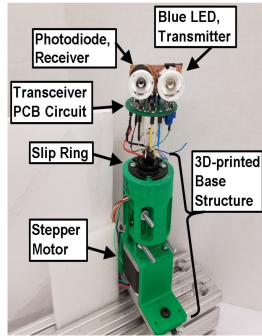


Fig. 12. Hardware components on each of the nodes.

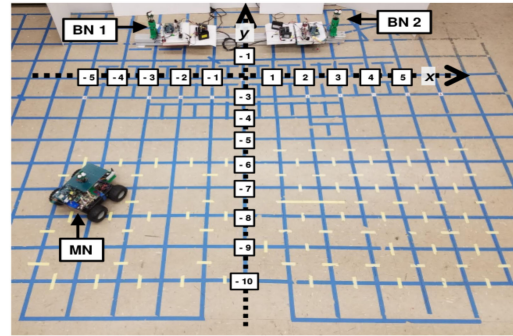


Fig. 13. Overhead view of the grid floor used in experiments.

transceiver to achieve  $360^\circ$  rotation, it was connected to the shaft of a stepper motor, which extended through the hollow center of a slip ring, allowing the wiring between the PCB circuit and the embedded controller to rotate freely with the motor. Fig. 12 illustrates the common hardware components on each node. The stepper motor was controlled through a Sparkfun Big Easy Driver, with the step resolution set to a rate of  $0.225^\circ/\text{step}$ . The orientation of the transceiver was determined by keeping count of the number of steps rotated and converting back and forth to degrees when needed.

The main processing unit for each node was an Intel Edison Board with an Arduino Expansion Board. It controlled the rotation of the stepper motor, transmission and reception of the LED signals as well as the processing of the Kalman filter data. The Intel Edison Boards had a 500 MHz Intel Atom dual-core processor with 1 GB of DDR3 RAM, and a built-in dual-band 2.4 GHz and 5 GHz Broadcom 43340 802.11 a/b/g/n Wi-Fi adapter.

The value for the systems' measurement noise covariance matrix  $R_k$  was calculated prior to the experiments by having the system try scanning the angles of the mobile node's position while the mobile node remained at a fixed location. Comparing the base node's measured position against this fixed position of the mobile node, errors for the  $x$  and  $y$  coordinates were computed and then used to generate a covariance matrix using the formula

$$R = \begin{bmatrix} R_{x,x} & R_{x,y} \\ R_{y,x} & R_{y,y} \end{bmatrix} = \frac{1}{K} \begin{bmatrix} \sum_{k=1}^K (\tilde{x}_k - \mu_x)^2 & \sum_{k=1}^K (\tilde{x}_k - \mu_x)(\tilde{y}_k - \mu_y) \\ \sum_{k=1}^K (\tilde{y}_k - \mu_y)(\tilde{x}_k - \mu_x) & \sum_{k=1}^K (\tilde{y}_k - \mu_y)^2 \end{bmatrix} \quad (11)$$

where  $K$  is the total number of measurements the base nodes captured,  $\tilde{x}$  and  $\tilde{y}$  are the magnitudes of the errors for the  $x$  and  $y$  coordinates, respectively, and  $\mu_x$  and  $\mu_y$  are the average errors among all of the captured measurements for  $x$  and  $y$ , respectively.

All of the experiments were contained within a grid structure laid out on the floor with blue painters tape, which followed

the grout line of the tiles. The side length of each tile's grout was approximately 23 cm and was used to represent 1 grid unit, which was the generic unit of length used in the experiments to measure motion and position, see Fig. 13. The area used in the experiments was defined as  $x \in [-6, 6]$ ,  $y \in [-11, 1]$  in grid units, where the  $x$ -axis and  $y$ -axis run parallel and perpendicular to the metal beam holding the base nodes, respectively.

The mobile node's orientation needs to be measured to compute the required rotation for the transceiver to establish the LOS by properly accommodating the rotation of the robot itself. The orientation was initially intended to be obtained via the magnetic compass of an inertial measurement unit mounted on the robot; however, the testing environment was surrounded by many sources of static magnetic interference and despite several attempts at calibrating and offsetting for these interferences, the resulting orientation output was too inconsistent and inaccurate to be useful in this application. We make an assumption that the magnetic compass approach will be more applicable when experimenting in an underwater environment. Consequently, for the experimental results shown here, the orientation data were captured with the use of NaturalPoint's OptiTrack motion tracking system, which used infrared cameras placed at strategic points above the perimeter of the grid, to illuminate and then capture the locations of reflective markers attached to a rectangular sheet of nontransparent acrylic mounted on the mobile node. During the experiments, OptiTrack would stream its tracked pose data to the mobile node over Wi-Fi using universal datagram protocol packets. This pose data also included the ground truth position of the MN, which was recorded into the node's data log purely for postprocessing analysis. The orientation data from the motion tracking system had an average error of  $0.2^\circ$ , which had negligible impact on the localization. However, in an outdoor (including underwater) environment, the orientation sensor (compass) will likely have larger errors, in which case one could use wider angle lens for the LED to increase its angular field of coverage but at the cost of its light intensity.

### B. Effect of Kalman Filter-Based Position Prediction

To further demonstrate the importance of Kalman filtering-based position prediction to the success of the proposed localization scheme, an alternative implementation of the system where

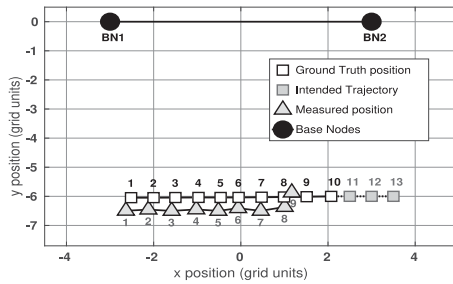


**Fig. 14.** Trajectory plot of one of the trials where prediction of the mobile node's position was not used for localizing. The system perceives its location to be the measured position computed from the bearing angles.

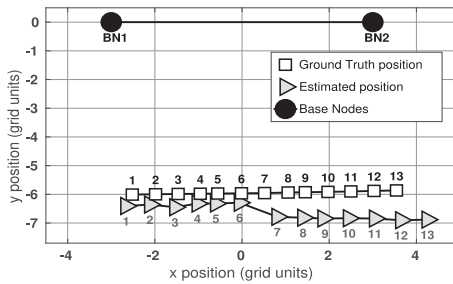


**Fig. 15.** Trajectory plot of one of the trials where Kalman filter-based prediction of the mobile node's position was used for localizing. The system perceives its location to be the Kalman filtering-based estimated position.

position prediction was not used was evaluated. In this implementation, the latest measured position, instead of the predicted position, was used as the basis for the LOS establishment for the mobile node and the base nodes. In particular, the previously measured position was used to generate the angles in which the base nodes and mobile node would use for centering the scans and LED light shining, respectively.

In this comparative experiment, the two versions were tasked to localize the mobile node as it traversed a short linear trajectory parallel to the base nodes, from  $[-3.0, -6.0]^T$  to  $[3.5, -6.0]^T$  in increments of 0.5 grid units in the positive  $x$  direction, a total of 13 steps. Three trials for each of the two versions were conducted. Figs. 14 and 15 show the trajectory plots from one of the trials of the versions without and with the use of the predicted positions, respectively. Both figures compare the position that the system perceives to be its location against the corresponding ground truth. For each position, the corresponding step number of the trajectory is placed next to it. For the version of the system without prediction all of the trials were unable to complete all 13 steps. Consequently, the trial shown in Fig. 14 can only show the ground truth positions for the steps at which it was able to localize, since it only receives the ground truth data with the orientation angle at the start of each step of the trajectory, and the remaining points are filled in by the intended points from the designed trajectory. On the other hand, all 3 trials of the version with prediction were able to complete all 13 steps of this trajectory.

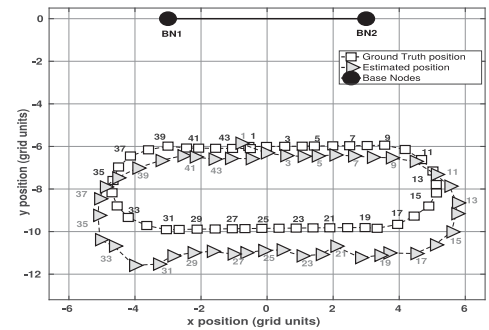


**Fig. 16.** Comparison of the ground truth and estimated positions of the experiment.

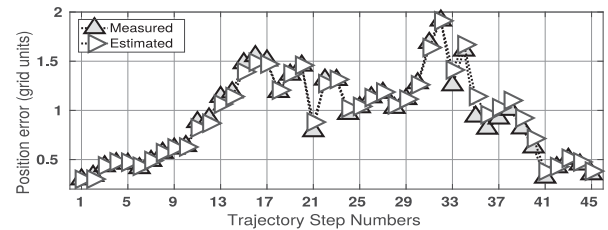


**Fig. 17.** Measured and estimated position error for each step of the trajectory.

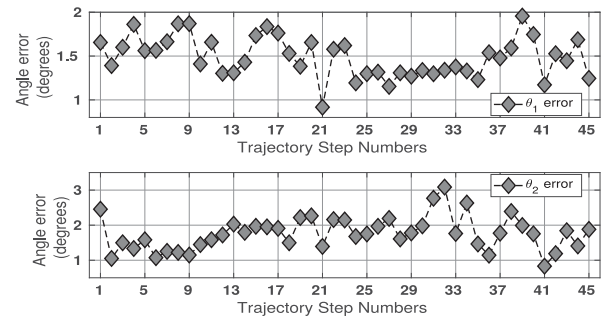


**Fig. 18.** Measured angle error is within the limits described by the simulation analysis.

### C. Results—Localization Around a Closed Loop

Two experimental trials of the system, with the mobile node following a simple loop trajectory, were conducted with the goal of showing the localization accuracy of the system when it was revisiting points of the trajectory it had already traversed and localized. Figs. 16–18 show the results obtained during one of these trials. Fig. 16 compares the trajectory points of ground truth and estimated positions. Fig. 17 shows the measured and estimated position errors, which are the errors between the measured (resp., Kalman filter-estimated) position and the ground truth position, for each step of the trajectory in the experiment. Both Figs. 16 and 17 show that the proposed method is capable of localizing the mobile robot around the full trajectory with an error of less than 2 grid units. These figures also indicate the system has more difficulty measuring the robot's position between the two turning portions of the trajectory in which the mobile node is the farthest away from the base nodes. Fig. 18 shows the measured angle error for both  $\theta_1$  and  $\theta_2$ , which

indicates that the measurement and filtering scheme is able to limit the measurement error within  $\pm 3^\circ$ .

## VI. CONCLUSION

This article has presented the algorithm design and system implementation for, to our best knowledge, the first LED-based localization scheme with a single-transmitter–single-receiver setup. A key idea exploited is the use of Kalman filtering, for predicting the position of the mobile node, to facilitate the establishment and maintenance of LOS. Simulation analysis has been presented on how much error in LOS measurement and knowledge of initial location that the system can withstand and still report sufficient localization accuracy. Experimentation shows the significance of the predicted position from the Kalman filter and how that allows the system to localize dynamically.

As part of our future work, we will explore measurement redundancies (by using more base nodes) to both tackle the singularity issue which arises when the MN is collinear with the Base Nodes and minimize the localization error stemming from the angle measurement errors. We have adopted a constant velocity model corrupted with noise to represent the motion of the robot. Such a seemingly simplistic model is a reasonable choice since the resulting scheme requires minimal knowledge about the motion dynamics of the robot. For future work, we will explore utilizing a rigid body motion model, with constant linear and angular velocities corrupted with noise, which could produce more accurate predictions of position (and orientation) for the robot. Finally, we plan to extend the approach to the full 3-D space and will further improve the hardware and advance the LED-based localization scheme for the use in the underwater setting.

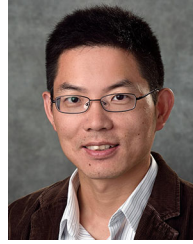
## REFERENCES

- [1] X. Tan, "Autonomous robotic fish as mobile sensor platforms: Challenges and potential solutions," *Marine Technol. Soc. J.*, vol. 45, no. 4, pp. 31–40, 2011.
- [2] A. Kim and R. Eustice, "Pose-graph visual SLAM with geometric model selection for autonomous underwater ship hull inspection," in *Proc. IEEE/RSJ Int. Conf. Intell. Robots Syst.*, Oct. 2009, pp. 1559–1565.
- [3] I. Cvišić, J. Česić, I. Marković, and I. Petrović, "SOFT-SLAM: Computationally efficient stereo visual simultaneous localization and mapping for autonomous unmanned aerial vehicles," *J. Field Robot.*, vol. 35, no. 4, pp. 578–595, Nov. 2018.
- [4] H. Chen, D. Sun, J. Yang, and J. Chen, "Localization for multirobot formations in indoor environment," *IEEE/ASME Trans. Mechatronics*, vol. 15, no. 4, pp. 561–574, Aug. 2010.
- [5] F. Aghili, "3D simultaneous localization and mapping using IMU and its observability analysis," *Robotica*, vol. 29, no. 6, pp. 805–814, Oct. 2011.
- [6] B. S. Cho, W. S. Moon, W. Seo, and K. R. Baek, "A dead reckoning localization system for mobile robots using inertial sensors and wheel revolution encoding," *J. Mech. Sci. Technol.*, vol. 25, no. 11, pp. 2907–2917, Nov. 2011.
- [7] R. Diamant and Y. Jin, "A machine learning approach for dead-reckoning navigation at sea using a single accelerometer," *IEEE J. Ocean. Eng.*, vol. 39, no. 4, pp. 672–684, Oct. 2014.
- [8] G. Dissanayake, S. Sukkariyah, E. Nebot, and H. Durrant-Whyte, "The aiding of a low-cost strapdown inertial measurement unit using vehicle model constraints for land vehicle applications," *IEEE Trans. Robot. Autom.*, vol. 17, no. 5, pp. 731–747, Oct. 2001.
- [9] M. S. Miah, J. Knoll, and K. Hevrdejs, "Intelligent range-only mapping and navigation for mobile robots," *IEEE Trans. Ind. Informat.*, vol. 14, no. 3, pp. 1164–1174, Mar. 2018.
- [10] K. Wang, Y. Liu, and L. Li, "A simple and parallel algorithm for real-time robot localization by fusing monocular vision and odometry/AHRS sensors," *IEEE/ASME Trans. Mechatronics*, vol. 19, no. 4, pp. 1447–1457, Aug. 2014.
- [11] F. Aghili and A. Salerno, "Driftless 3-D attitude determination and positioning of mobile robots by integration of IMU with two RTK GPSs," *IEEE/ASME Trans. Mechatronics*, vol. 18, no. 1, pp. 21–31, Feb. 2013.
- [12] G. Rui and M. Chitre, "Cooperative multi-AUV localization using distributed information filter," in *Proc. IEEE/OES Auton. Underwater Veh.*, Nov. 2016, pp. 206–212.
- [13] L. E. Emokpae, S. DiBenedetto, B. Poteiger, and M. Younis, "UREAL: Underwater reflection-enabled acoustic-based localization," *IEEE Sensors J.*, vol. 14, no. 11, pp. 3915–3925, Nov. 2014.
- [14] B. Tian, F. Zhang, and X. Tan, "Design and development of an LED-based optical communication system for autonomous underwater robots," in *Proc. IEEE/ASME Int. Conf. Adv. Intell. Mechatronics*, Jul. 2013, pp. 1558–1563.
- [15] P. B. Solanki, M. Al-Rubaia, and X. Tan, "Extended Kalman filter-aided alignment control for maintaining line of sight in optical communication," in *Proc. Amer. Control Conf.*, Jul. 2016, pp. 4520–4525.
- [16] H. Brundage, "Designing a wireless underwater optical communication system," Master's thesis, Dept. Mechanical Eng., Massachusetts Inst. Technol., Cambridge, MA, USA, 2010.
- [17] M. Doniec, "Autonomous underwater data muling using wireless optical communication and agile AUV control," Ph.D. dissertation, Dept. Elect. Eng. Comput. Sci., Massachusetts Institute Technol., Cambridge, MA, USA, 2013.
- [18] D. Anguita, D. Brizzolara, and G. Parodi, "Building an underwater wireless sensor network based on optical: Communication: Research challenges and current results," in *Proc. 3rd Int. Conf. Sensor Technol. Appl.*, Jun. 2009, pp. 476–479.
- [19] D. Anguita, D. Brizzolara, and G. Parodi, "Optical wireless communication for underwater wireless sensor networks: Hardware modules and circuits design and implementation," in *Proc. OCEANS*, Sep. 2010, pp. 1–8.
- [20] I. C. Rust and H. H. Asada, "A dual-use visible light approach to integrated communication and localization of underwater robots with application to non-destructive nuclear reactor inspection," in *Proc. IEEE Int. Conf. Robot. Autom.*, May 2012, pp. 2445–2450.
- [21] J. A. Simpson, B. L. Hughes, and J. F. Muth, "Smart transmitters and receivers for underwater free-space optical communication," *IEEE J. Sel. Areas Commun.*, vol. 30, no. 5, pp. 964–974, Jun. 2012.
- [22] M. Al-Rubaia, "Design and development of an LED-based optical communication system," Master's thesis, Dept. Elect. Comput. Eng., Michigan State Univ., East Lansing, MI, USA, 2015.
- [23] P. B. Solanki, M. Al-Rubaia, and X. Tan, "Extended Kalman filter-based active alignment control for LED optical communication," *IEEE/ASME Trans. Mechatronics*, vol. 23, no. 4, pp. 1501–1511, Aug. 2018.
- [24] K. Qiu, F. Zhang, and M. Liu, "Let the light guide us: VLC-based localization," *IEEE Robot. Autom. Mag.*, vol. 23, no. 4, pp. 174–183, Dec. 2016.
- [25] N. T. Nguyen, N. H. Nguyen, V. H. Nguyen, K. Sripimanwat, and A. Suebsomran, "Improvement of the VLC localization method using the extended Kalman filter," in *Proc. TENCON IEEE Region 10 Conf.*, Oct. 2014, pp. 1–6.
- [26] J. N. Greenberg and X. Tan, "Efficient optical localization for mobile robots via Kalman filtering-based location prediction," in *Proc. ASME Dyn. Syst. Control Conf.*, Oct. 2016, Paper DSCC2016-9917.
- [27] J. N. Greenberg and X. Tan, "Kalman filtering-aided optical localization of mobile robots: System design and experimental validation," in *Proc. ASME Dyn. Syst. Control Conf.*, Oct. 2017, Paper DSCC2017-5368.
- [28] R. E. Kalman, "A new approach to linear filtering and prediction problems," *Trans. ASME—J. Basic Eng.*, vol. 82, no. Series D, pp. 35–45, 1960.
- [29] S. Panzneri, F. Pascucci, and G. Ulivi, "An outdoor navigation system using GPS and inertial platform," *IEEE/ASME Trans. Mechatronics*, vol. 7, no. 2, pp. 134–142, Jun. 2002.
- [30] D. Bouvet and G. Garcia, "Improving the accuracy of dynamic localization systems using RTK GPS by identifying the GPS latency," in *Proc. IEEE Int. Conf. Robot. Autom. Millennium Conf.*, Apr. 2000, pp. 2525–2530.
- [31] J. Meguro, J. Takiguchi, Y. Amano, and T. Hashizume, "3D reconstruction using multibaseline omnidirectional motion stereo based on GPS/dead-reckoning compound navigation system," *Int. J. Robot. Res.*, vol. 26, no. 6, pp. 625–636, Jun. 2007.



**Jason Neil Greenberg** (Student Member, IEEE) received the B.S. degree in computer engineering from the State University of New York (SUNY) at New Paltz, New York, NY, USA, in 2012. He is currently working toward the Ph.D. degree in electrical and computer engineering with Michigan State University, East Lansing, MI, USA.

His research interest includes localization of a mobile robot using the bearing angle from an LED-based optical communication system for underwater applications.



**Xiaobo Tan** (Fellow, IEEE) received the B.Eng. and M.Eng. degrees in automatic control from Tsinghua University, Beijing, China, in 1995 and 1998, respectively, and the Ph.D. degree in electrical and computer engineering from the University of Maryland, College Park, MD, USA, in 2002.

He is currently an MSU Foundation Professor with the Department of Electrical and Computer Engineering, Michigan State University (MSU), East Lansing, MI, USA. His research interests include development, dynamic modeling, control, and applications of smart material systems, soft robots, and underwater robots.

Dr. Tan currently serves as a Senior Editor for the IEEE/ASME TRANSACTIONS ON MECHATRONICS and an Associate Editor for *Automatica*. He has coauthored one book (*Biomimetic Robotic Artificial Muscles*) and more than 250 peer-reviewed journal and conference papers, and holds three US patents. He is a Fellow of ASME, and a recipient of the NSF CAREER Award (2006), MSU Teacher-Scholar Award (2010), MSU College of Engineering Withrow Distinguished Scholar Award (2018), Distinguished Alumni Award from the Department of Electrical and Computer Engineering, University of Maryland (2018), and several best paper awards.